remote sensing

MDPI

Article

LiDAR-Constrained Multi-Temporal UAV Monitoring of Glacier Terminus Retreat and Secondary Landslide Evolution at Hailuogou Glacier, Mt. Gongga, China

Jiajun Zhang [1,2], Yixiang Du [3], Weike Zhang [4], Qian Zhou [5], Bo Zhang [6], Mingjun Li [3], Yuhao Yang [1], Liying Huang [1] and Jialun Cai [1,2,*]

[1] School of Environment and Resources, Southwest University of Science and Technology, Mianyang 621010, China; 7220240176@mails.swust.edu.cn (J.Z.); yangyuhao@mails.swust.edu.cn (Y.Y.); 7220250253@mails.swust.edu.cn (L.H.)
[2] Mianyang Science and Technology City Branch, National Remote Sensing Center, Mianyang 621010, China
[3] Sichuan Zhentong Inspection Co., Ltd., Mianyang 621000, China; scztjc@163.com (Y.D.); kinglee699@163.com (M.L.)
[4] The Land Surveying and Mapping Center, The Third Geodetic Surveying Brigade of the Ministry of Natural Resources of China, Chengdu 610058, China; jay9787@163.com
[5] Hunan Institute of Remote Sensing Geological Survey and Monitoring, Changsha 410015, China; zhouqian@hnygs.com
[6] Institute of Mountain Hazards and Environment, Chinese Academy of Sciences and Ministry of Water Resources, Chengdu 610041, China; rsbozh@imde.ac.cn
* Correspondence: rscai@swust.edu.cn

Highlights

What are the main findings?

- The monitored glacier terminus lost 45.5% of its area between 2018 and 2022, with spatially uneven retreat.
- The adjacent landslide shifted from deposition-dominated change to erosion-dominated change during July 2020–August 2022.

What are the implications of the main findings?

- LiDAR-constrained multi-temporal UAV surveys enable integrated quantification of glacier retreat and adjacent landslide erosion and deposition.
- The observed glacier–landslide covariation highlights the value of joint monitoring for hazard assessment in evolving glacier-margin environments.

Abstract

Joint quantification of glacier terminus change and adjacent secondary landslide evolution can be challenging when multi-temporal UAV datasets lack a consistent absolute spatial reference, thereby limiting robust assessment of their stage-dependent covariation. This study investigated the Hailuogou glacier terminus and the Laoguanjingtai (LGJT) landslide using six UAV photogrammetric surveys acquired between 2018 and 2022 and synchronous airborne light detection and ranging (LiDAR) data from 2022. LiDAR reference constraints and elevation-residual assessment over relatively stable terrain supported multi-temporal digital elevation model (DEM) differencing. The glacier terminus area decreased from 2.63×10^5 m^2 to 1.43×10^5 m^2, representing a reduction of 45.5%. From July 2020 to August 2022, the glacier volume ablation rate reached 1.00×10^6 m^3 a^{-1}. Meanwhile, the LGJT landslide shifted from deposition-dominated adjustment from 2018 to 2019 to erosion-dominated material export after July 2020, when its erosion rate reached 3.73×10^5 m^3 a^{-1} and its net volume change rate decreased to -3.39×10^5 m^3 a^{-1}. Annualized rates across five unequal intervals showed positive covariation between glacier ablation

Check for updates

Academic Editor: Kevin Tansey

Received: 12 September 2026
Revised: 29 October 2026
Accepted: 5 November 2026
Published: 8 November 2026

Copyright: © 2026 by the authors. Licensee MDPI, Basel, Switzerland. This article is an open access article distributed under the terms and conditions of the Creative Commons Attribution (CC BY) license.

and landslide erosion and negative covariation with net landslide volume change. These exploratory associations, together with the spatial concentration of elevation change near the glacier–landslide margin, are consistent with a geomorphic linkage. The LiDAR-constrained UAV workflow provides a practical basis for integrated monitoring of glacier retreat and adjacent sediment redistribution.

Keywords: Hailuogou glacier; glacier ablation; secondary landslide; airborne LiDAR; UAV photogrammetry

1. Introduction

Mountain glaciers are sensitive indicators of climate change and play a key role in regulating regional freshwater resources; consequently, their dynamic evolution has received increasing scientific attention [1,2]. In recent decades, most glaciers in western China and around the Tibetan Plateau have experienced substantial area shrinkage, mass loss, and terminus retreat under global warming. Persistent changes in glacier mass balance not only alter downstream runoff supply but also modify slope stability conditions and the evolution of paraglacial landscapes [3,4]. Glacier retreat is not limited to a simple reduction in ice extent. It can also alter the boundary conditions of adjacent slopes through debuttressing, moraine exposure, meltwater pathway reorganization, and channel erosion. Recent studies of high mountain hazards show that rock-ice avalanches, landslides, and glacial-lake outburst floods can initiate abruptly and evolve into strongly amplified multihazard cascades in deglaciating mountain environments [5–7]. Therefore, landslide monitoring in glacier ablation zones requires coordinated quantification of glacier boundary change, elevation loss, and the redistribution of slope material.

Modern remote sensing techniques provide multiscale and multisource observations for monitoring glacier dynamics and assessing associated high mountain hazards [8,9]. Satellite remote sensing is well suited to regional-scale delineation of glacier outlines and estimation of surface velocity and geodetic mass change. However, detailed observations in steep alpine valleys remain challenging: optical satellite imagery is frequently affected by cloud cover and terrain shadows, whereas complex viewing geometries, topographic occlusion, and limited spatial resolution can obscure localized changes. In recent years, rapid advances in unmanned aerial vehicle (UAV) photogrammetry have enabled the flexible acquisition of centimetre- to decimetre-resolution digital orthophoto maps (DOMs) and digital elevation models (DEMs). Consequently, multi-temporal UAV surveys have become valuable for resolving fine-scale changes in glacier termini, mapping landslide boundary migration and surface deformation, and quantifying microtopographic adjustments in proglacial channels [10–14].

For site-specific landslide investigations, UAV photogrammetry, near-surface geophysical techniques, and airborne light detection and ranging (LiDAR) have increasingly been integrated to delineate landslide boundaries and subsurface structures, quantify surface deformation, reconstruct high-resolution topography, estimate source area volumes, and support landslide stability and hazard assessments [15–24]. Nevertheless, long-term multi-temporal UAV monitoring in steep, complex glacier ablation terrain still faces two major technical difficulties. First, because glacier and moraine landforms are continuously evolving, long-term deployment of ground control points (GCPs) is difficult, and DEMs of difference (DoDs) are therefore susceptible to systematic vertical bias. Second, the dynamic links between glacier ablation and the erosion and deposition of the landslide are challenging to quantify through a single metric; thus, a comprehensive analysis integrating

correlation coefficients, DOM interpretation, DoD spatial pattern evaluation, and dynamic geomorphic boundary extraction is required.

To address these issues, this study investigated the contact zone between the Laoguanjingtai (LGJT) landslide and the Hailuogou glacier terminus on Mt. Gongga. A LiDAR-constrained multi-temporal UAV workflow was applied to quantify glacier retreat and adjacent landslide erosion and deposition and assess their spatiotemporal covariation and geomorphic context.

2. Materials and Methods

2.1. Study Area

Hailuogou Glacier is located on the eastern slope of Mt. Gongga (Figure 1) and is a typical maritime glacier at low altitude. It is characterized by a large elevation range, abundant precipitation, intense ablation, and extensive supraglacial debris cover. Long-term observations and previous studies have shown that Hailuogou Glacier has undergone continuous and accelerating retreat in recent decades [25,26]. Long-term monitoring of maritime glaciers on Mt. Gongga and multi-source remote sensing reconstructions from 1974 to 2020 further confirm substantial and irreversible changes in terminus position, total area, and ablation zone surface morphology [27–29]. The slope adjacent to the former viewing platform plank road lies close to the glacier terminus. Historical records indicate repeated landslide hazards in this area, with severe erosion and damage to plank road facilities, showing a distinct secondary landslide response under glacier retreat conditions [30].

For quantitative analysis of glacier ablation and landslide activity, the study area was divided into a glacier terminus zone, a landslide zone, and relatively stable reference areas. The glacier terminus zone was used to extract glacier boundaries, area loss, and ablation volume. The landslide zone was used to calculate volume changes of the LGJT landslide. Reference areas were selected around roads, platforms, and artificial structures that were outside areas visibly affected by glacier ablation and channel erosion and showed comparatively limited morphological change in multi-temporal DOMs. These areas were used to estimate DEM differencing errors and systematic elevation residuals between adjacent surveys.

2.2. Data Sources

Six UAV image datasets acquired from May 2018 to August 2022 were used in this study. The main UAV survey parameters and related processing parameters are listed in Table 1. These datasets meet the requirements for glacier terminus interpretation and landslide geomorphology identification. Information on the survey platforms, sensors, and positioning modes is provided in Table 2.

The airborne LiDAR data acquired synchronously in 2022 served as the external spatial reference. These data were used to evaluate and control relative DEM differencing uncertainty across multi-temporal UAV DEMs through consistency checks between the UAV and LiDAR data, the extraction of three-dimensional reference points, and the application of LoD_{95} thresholds in stable areas. Specifically, the LiDAR data and the 2022 high-precision oblique photogrammetric model were jointly used to identify stable features visible across survey periods, providing control constraints for aerial triangulation of the single-camera UAV images acquired from 2018 to 2020. Meanwhile, the LiDAR DEM was used as the 2022 topographic dataset for subsequent DoD calculation and to validate the vertical consistency of the synchronous UAV DEM over stable areas.

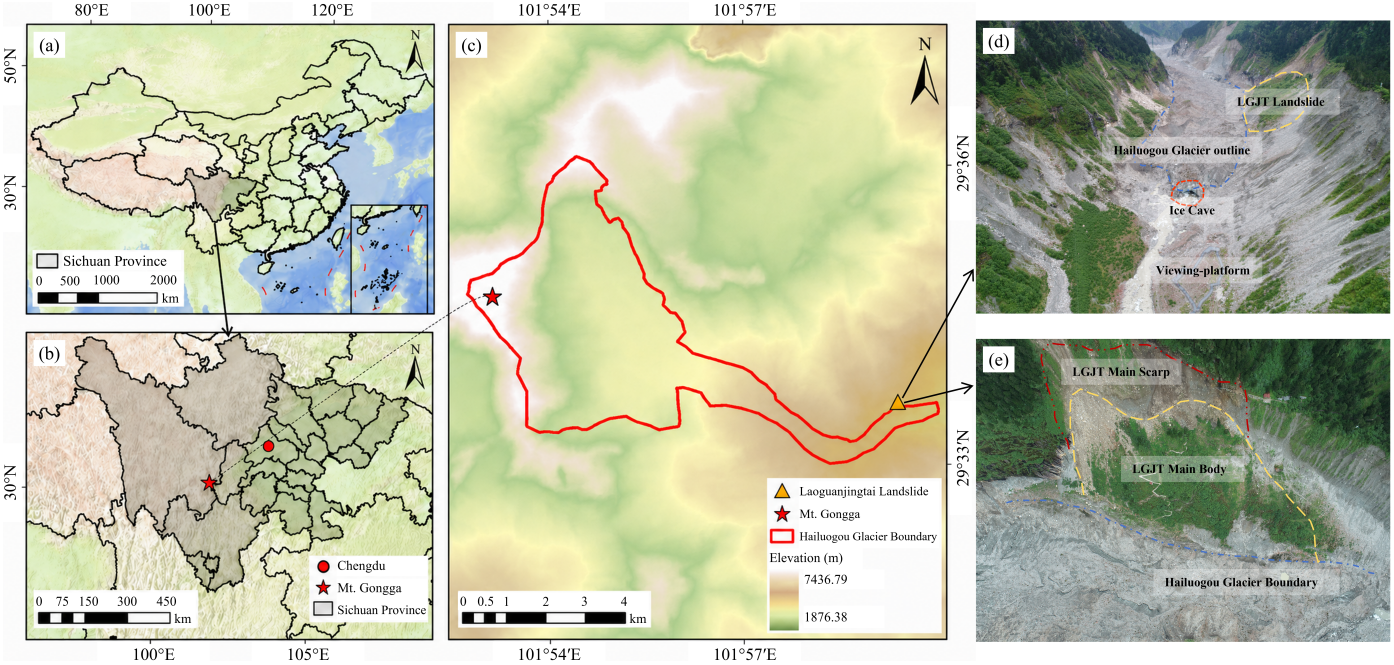

Figure 1. Location and field setting of the study area. (**a**) Location in China; (**b**) regional setting; (**c**) spatial relationship among Hailuogou Glacier, the LGJT landslide, and Mt. Gongga; (**d**) Glacier terminus: red and yellow dashed outlines indicate the ice cave and LGJT landslide, respectively; (**e**) adjacent landslide: red and yellow dashed lines indicate the LGJT Main Scarp and LGJT Main Body, respectively. Blue dashed lines in both panels indicate the Hailuogou Glacier boundary.

Table 1. UAV photogrammetry parameters.

Parameter	15 May 2018	9 December 2018	15 May 2019	29 June 2019	18 July 2020	3 August 2022
Captured images	500	998	1529	1221	1407	9305
Used images	246	443	278	284	360	1520
Flight height (m)	300–350	300–350	300–350	300–350	300–350	300–350
Photogrammetric overlap (forward/side)	80%/70%	80%/70%	80%/70%	80%/70%	80%/70%	80%/70%
Ground sampling distance (cm/pixel)	10.42	6.85	8.71	10.76	8.80	3.30
Coverage area (km^2)	3.235	3.648	3.794	3.605	4.141	6.405
Reprojection RMS (pixel)	0.52	0.47	0.51	0.56	0.46	0.44
Overall control point reprojection RMS (pixel)	0.99	0.72	0.43	0.76	0.41	-

Table 2. Supplementary survey equipment and acquisition information.

Parameter	2018–2020 UAV Photogrammetry	2022 Oblique Photogrammetry	2022 LiDAR
Platform	DJI MATRICE 600 Pro	DJI MATRICE 600 Pro	CHCNAV BB4
Sensor	DJI FC6310	Sony ILCE-6000	CHCNAV AU1300

Table 2. *Cont*.

Parameter	2018–2020 UAV Photogrammetry	2022 Oblique Photogrammetry	2022 LiDAR
Image size (pixels)	5472 × 3648	6000 × 4000	-
Focal length (mm)	8.8	27 (S) 43 (A, D, W, X)	-
Positioning mode	RTK	PPK	PPK
Point density (points m^{-2})	-	-	39.01

S, A, D, W, and X denote the camera channels. RTK and PPK denote real-time kinematic and post-processed kinematic positioning, respectively. The point density reported in the table is the mean all-return point density of the clipped LiDAR point cloud.

2.3. Data Processing and Analysis Workflow

The technical workflow consisted of three steps. First, the 2022 airborne LiDAR data were used to establish a common spatial reference and assess the relative vertical consistency of the synchronous UAV DEM over reference areas. Second, LiDAR-constrained reference features were introduced into the aerial triangulation of the UAV images acquired from 2018 to 2020 so as to construct a long-term DEM series under a common reference frame, followed by DoD analysis using reference-area LoD_{95} thresholds. Third, glacier area retreat, ablation volume, landslide erosion, and landslide deposition were extracted from DOM boundary changes and DoD spatial patterns. Stage-dependent glacier–landslide covariation was then discussed using the statistical and geomorphic evidence. The complete workflow is shown in Figure 2.

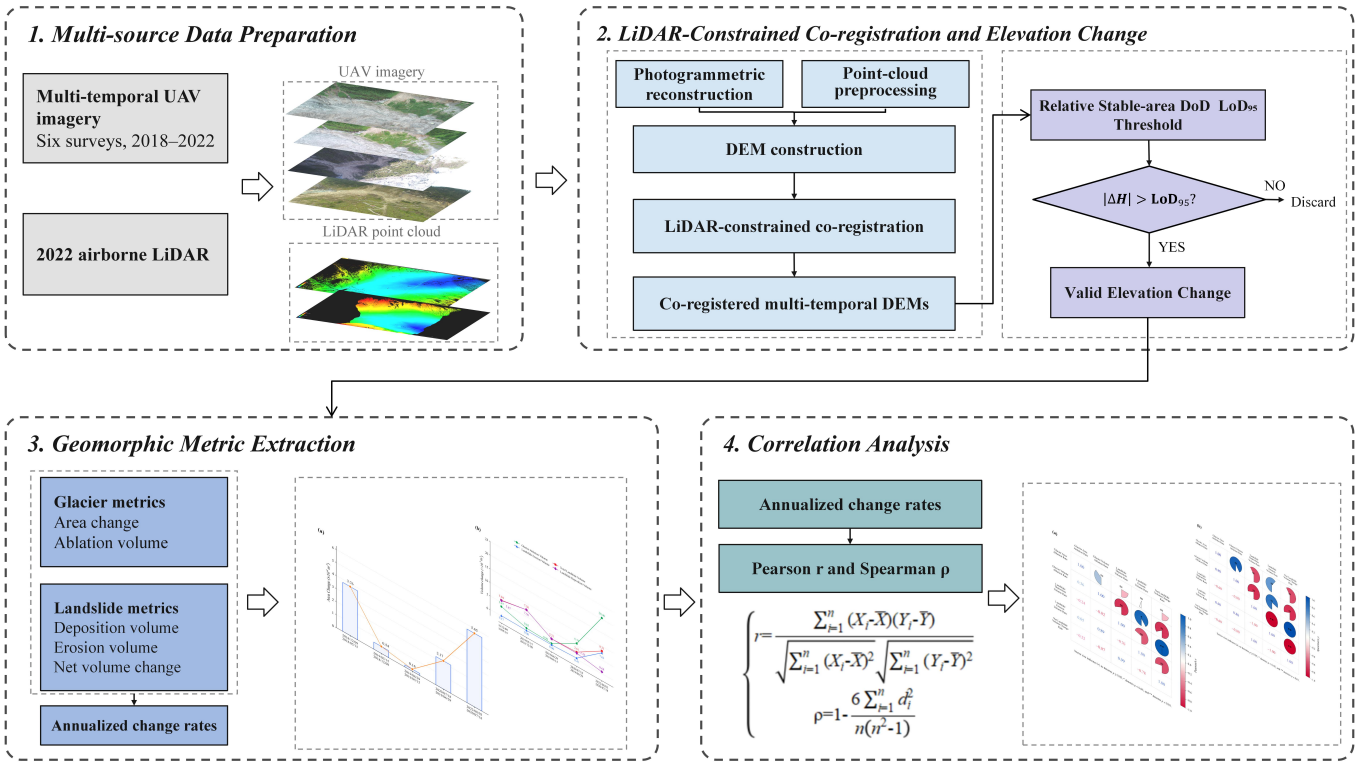

Figure 2. LiDAR-constrained workflow for multi-temporal UAV topographic change monitoring and analysis.

2.3.1. Long-Term DEM Construction Constrained by LiDAR

In alpine environments without field-measured GCPs, long-term photogrammetry may introduce systematic geometric distortion and vertical bias because of insufficient absolute reference constraints. In this study, a high-precision reference DEM was generated from the 2022 airborne LiDAR data and compared with the synchronous UAV DEM over overlapping stable areas. As shown in Table 3, the root mean square error (RMSE), normalized median absolute deviation (NMAD), and mean difference between the 2022 UAV DEM and LiDAR DEM over stable areas were 0.218 m, 0.144 m, and 0.087 m, respectively, indicating good vertical consistency over stable terrain.

Table 3. Vertical accuracy assessment between the UAV DEM and LiDAR DEM over stable areas.

Comparison	Pixels	Mean (m)	Median (m)	Std (m)	RMSE (m)	NMAD (m)	LoD_{95} RMSE (m)
2022 UAV–LiDAR	601,386	0.087	0.096	0.200	0.218	0.144	0.427

Four reference locations associated with the parking area, flower bed, viewing-platform area, and cableway foundation were selected to provide spatial constraints for the historical UAV surveys (Figure 3). Close-up views of the available reference features from all six surveys during 2018–2022 are provided in Figure S1. Their three-dimensional coordinates were derived from the 2022 LiDAR data and oblique photogrammetric model and incorporated into the aerial triangulation of the 2018–2020 imagery. Because the boardwalk had not yet been constructed in 2018, the reference location associated with it was unavailable, and only the other three locations were used for the 2018 aerial triangulation. The five UAV surveys conducted during 2018–2020 achieved ground sampling distances of approximately 7–11 cm, providing sufficient spatial detail for visual identification of the available reference features. Selection focused on recognizable ground features with comparatively limited morphological change. Although minor creep or settlement cannot be excluded over the monitoring period, these features were considered relatively reliable spatial references compared with the actively changing glacier margin and adjacent unconsolidated surfaces. They therefore provided practical constraints for placing the historical reconstructions within a common spatial reference.

2.3.2. Error Threshold and Volume Calculation

The point clouds generated after UAV bundle adjustment and the 2022 airborne LiDAR point cloud were used as the topographic data sources. Ground points were extracted using the simple morphological filter (SMRF) [31], with the following parameter settings: slope = 0.25, window = 18.0, threshold = 0.5, and scalar = 1.25. Residual vegetation and water body noise were removed manually. The resulting ground points were then converted into DEMs, spatially clipped, co-registered, and resampled to a common spatial resolution of 0.25 m.

To reduce the influence of DEM noise and systematic vertical bias on volume estimates, elevation residuals over stable areas were used to determine the detection limit for each pair of adjacent DEMs. The stable area residual statistics included the mean, standard deviation, RMSE, and NMAD. For stable area residuals e_i, NMAD was calculated as $\mathrm{NMAD} = 1.4826\,\mathrm{median}(|e_i - \mathrm{median}(e)|)$. Because NMAD is relatively insensitive to a small number of outliers, it was used to construct a robust threshold for the minimum detectable elevation change:

$$\mathrm{LoD}_{95} = 1.96\sqrt{\mathrm{NMAD}_{t1}^2 + \mathrm{NMAD}_{t2}^2}. \quad (1)$$

Where $NMAD_{t1}$ and $NMAD_{t2}$ represent the vertical uncertainties of the DEMs acquired at $t1$ and $t2$, respectively. The LoD_{95} value represents the minimum detectable elevation change at the 95% confidence level and was calculated separately for each pair of adjacent DEMs.

Systematic vertical bias was further corrected using the mean elevation difference over stable areas. The bias-corrected and threshold-filtered elevation changes were calculated as follows:

$$\begin{cases} \Delta h_i = H_{t2}^{(i)} - H_{t1}^{(i)} - \mu_s, \\ \Delta h_i^* = \begin{cases} \Delta h_i, & |\Delta h_i| > \mathrm{LoD}_{95}, \\ 0, & |\Delta h_i| \le \mathrm{LoD}_{95}. \end{cases} \end{cases} \tag{2}$$

Where $H_{t1}^{(i)}$ and $H_{t2}^{(i)}$ are the elevations of pixel i in the earlier and later DEMs, respectively; μ_s is the mean elevation difference over the stable areas; Δh_i is the bias-corrected elevation difference; and Δh_i^* is the effective elevation change after application of the LoD_{95} threshold. Pixels with elevation changes not exceeding the threshold were regarded as non-significant and were excluded from subsequent volume calculations. Positive values of Δh_i^* indicate deposition, burial, or local uplift, whereas negative values indicate erosion, sliding, or glacier ablation.

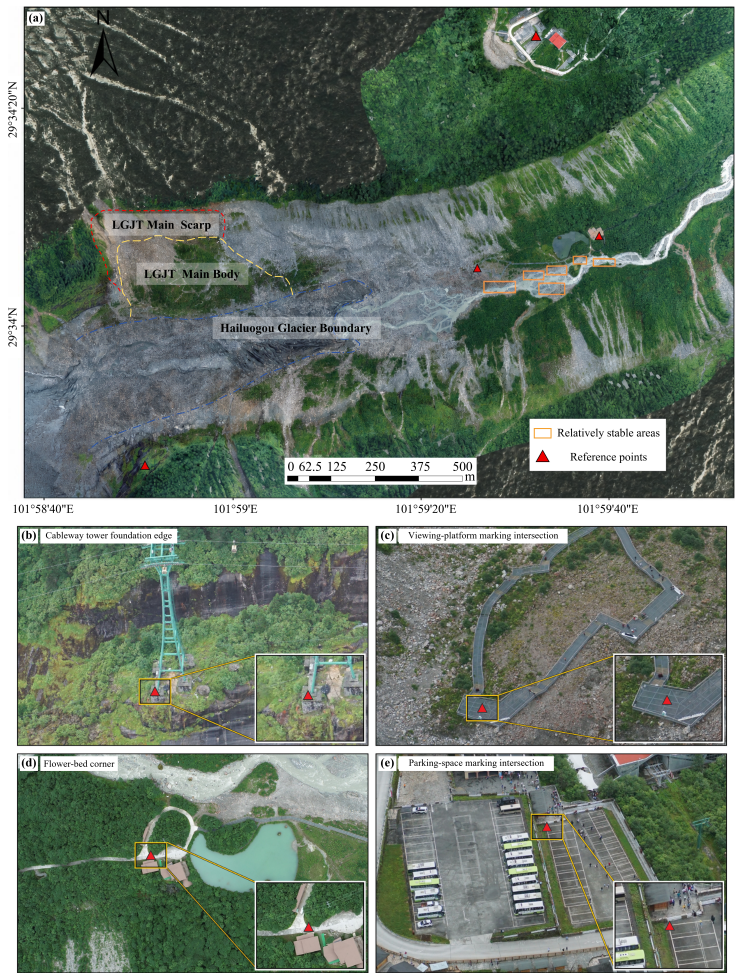

Figure 3. Reference locations and relatively stable areas. (**a**) Spatial distribution relative to the glacier terminus and the LGJT landslide. Red, yellow, and blue dashed lines indicate the LGJT Main Scarp, LGJT Main Body boundary, and Hailuogou Glacier boundary, respectively. (**b**) Cableway foundation; (**c**) viewing-platform area; (**d**) flower-bed corner; (**e**) parking-space markings.

2.3.3. Change Metrics and Correlation Analysis

Glacier boundaries and landslide change areas were manually delineated by jointly interpreting multi-temporal DOMs, DEMs, and three-dimensional photogrammetric models. Mapping considered the combined appearance and morphology of debris-covered ice, moraine deposits, exposed ice cliffs, supraglacial debris, meltwater channels, and landslide scarps rather than relying on surface color alone. DEM relief and three-dimensional views supported interpretation where debris-covered ice and adjacent sediment had similar optical appearances. The glacier analysis was restricted to the terminus zone adjacent to the LGJT landslide, not the entire glacier. Straight segments used to close the selected analysis polygons do not necessarily represent natural glacier margins or landslide scarps.

Boundary migration was interpreted from the DOM overlays, whereas DoDs measure elevation differences at fixed horizontal locations. Positive and negative differences were interpreted as surface raising and lowering, with deposition, erosion, and ablation assessed from their geomorphic context. Boundary interpretation remains uncertain in shadowed, debris-covered, or rapidly reworked areas.

The glacier terminus area at each survey time, the area loss between adjacent surveys, and the corresponding annualized area ablation rate were calculated as follows:

$$\begin{cases} A_t = A_0 \sum\limits_{i \in \Omega_g} M_t^{(i)}, \\ \Delta A = A_{t1} - A_{t2}, \\ R_A = \dfrac{\Delta A}{\Delta t}. \end{cases} \tag{3}$$

Where A_t is the glacier terminus area at survey time t; $A_0 = 0.0625$ m^2 is the area of one 0.25 m × 0.25 m pixel; Ω_g is the glacier terminus analysis domain; and $M_t^{(i)}$ is the binary glacier mask of pixel i, with values of 1 and 0 representing glacier and non-glacier areas, respectively. The terms ΔA and R_A represent glacier area loss and its annualized rate, respectively, and Δt is the monitoring interval in years. Under this definition, a positive value of ΔA indicates a reduction in glacier terminus area.

Glacier ablation volume, landslide deposition volume, landslide erosion volume, net landslide volume change, and their corresponding annualized rates were calculated from the effective elevation changes as follows:

$$\begin{cases} V_{\text{abl}} = A_0 \sum\limits_{\substack{i \in \Omega_g \\ \Delta h_i^* < 0}} |\Delta h_i^*|, \\ V_{\text{dep}} = A_0 \sum\limits_{\substack{i \in \Omega_l \\ \Delta h_i^* > 0}} \Delta h_i^*, \\ V_{\text{ero}} = A_0 \sum\limits_{\substack{i \in \Omega_l \\ \Delta h_i^* < 0}} |\Delta h_i^*|, \\ V_{\text{net}} = V_{\text{dep}} - V_{\text{ero}}, \\ R_{V,k} = \dfrac{V_k}{\Delta t}, \qquad k \in \{\text{abl}, \text{dep}, \text{ero}, \text{net}\}. \end{cases} \tag{4}$$

Where Ω_g and Ω_l denote the glacier terminus and landslide analysis domains, respectively. The terms V_{abl}, V_{dep}, and V_{ero} represent glacier ablation volume, landslide deposition volume, and landslide erosion volume, respectively. Glacier ablation and landslide erosion are reported as positive magnitudes. In contrast, V_{net} is the algebraic landslide volume change, for which positive and negative values indicate net deposition and net erosion

or outward mass transport, respectively. The annualized volume change rate $R_{V,k}$ was obtained by dividing the corresponding volume term by the monitoring interval Δt.

Correlation analysis was performed using five annualized indicators: glacier area ablation rate, glacier volume ablation rate, landslide deposition volume rate, landslide erosion volume rate, and net landslide volume change rate. Both the Pearson product-moment correlation coefficient and the Spearman rank correlation coefficient were calculated:

$$\begin{cases} r = \dfrac{\sum_{i=1}^{n}\left(X_i - \overline{X}\right)\left(Y_i - \overline{Y}\right)}{\sqrt{\sum_{i=1}^{n}\left(X_i - \overline{X}\right)^2}\sqrt{\sum_{i=1}^{n}\left(Y_i - \overline{Y}\right)^2}}, \\ \rho = 1 - \dfrac{6\sum_{i=1}^{n} d_i^2}{n(n^2-1)}. \end{cases} \quad (5)$$

Where r and ρ are the Pearson and Spearman correlation coefficients, respectively; X_i and Y_i are the paired annualized change rate indicators for monitoring interval i; $\overline{X}$ and $\overline{Y}$ are their respective means; d_i is the difference between the paired ranks; and $n = 5$ is the number of adjacent monitoring intervals. The expression for ρ applies when no tied ranks are present; if tied values occur, average ranks should be assigned before calculating the Spearman coefficient.

Only five paired monitoring intervals were available ($n = 5$), limiting the statistical power and robustness of the correlation analysis. Annualization scales interval totals by duration but does not eliminate differences in seasonal and event coverage across the 45–746-day intervals. Accordingly, Pearson and Spearman correlation coefficients were treated as exploratory indicators of covariation and interpreted alongside DoD spatial patterns, DOM-derived boundary changes, and glacier and landslide geomorphic processes, rather than as stand-alone evidence of causality.

3. Results

3.1. Glacier Terminus Area Retreat and Ablation Volume Change

From May 2018 to August 2022, the delineated glacier terminus monitoring zone underwent substantial retreat, with its area decreasing from 2.63×10^5 m^2 to 1.43×10^5 m^2. This corresponds to a cumulative reduction of approximately 1.20×10^5 m^2 and an overall retreat ratio of 45.5%. The area loss sequence shown in Figure 4a indicates pronounced temporal variability: relatively rapid retreat occurred in 2018, followed by limited planimetric change during 2019, renewed retreat after June 2019, and the greatest area loss from July 2020 to August 2022. Glacier ablation volume exhibited a broadly similar but more pronounced late-stage increase (Figure 4b), reaching 2.046×10^6 m^3 during the final interval. These cumulative maxima were recorded during the longest monitoring interval. Nevertheless, the final interval also had the highest annualized glacier volume loss, whereas annualized glacier area loss peaked in 2018 (Table 4). This contrast is consistent with substantial late-stage surface lowering and highlights differing temporal patterns of glacier area and volume loss.

Figure 4b also reveals a clear transition in the volumetric evolution of the adjacent LGJT landslide. Deposition dominated during the earlier monitoring intervals, whereas erosion increased sharply from July 2020 to August 2022 and substantially exceeded deposition. This transition indicates a shift from material accumulation to enhanced erosion and outward sediment transport. The multi-temporal boundaries in Figure 5 further demonstrate that

glacier retreat was spatially heterogeneous. The greatest boundary displacement occurred in the low-lying frontal sector and along the lateral margin adjacent to the landslide zone, while several upper and lateral segments remained comparatively stable. The boundary patterns and interval totals indicate spatially uneven retreat and greater cumulative late-stage change; they do not resolve when individual changes occurred within the final interval.

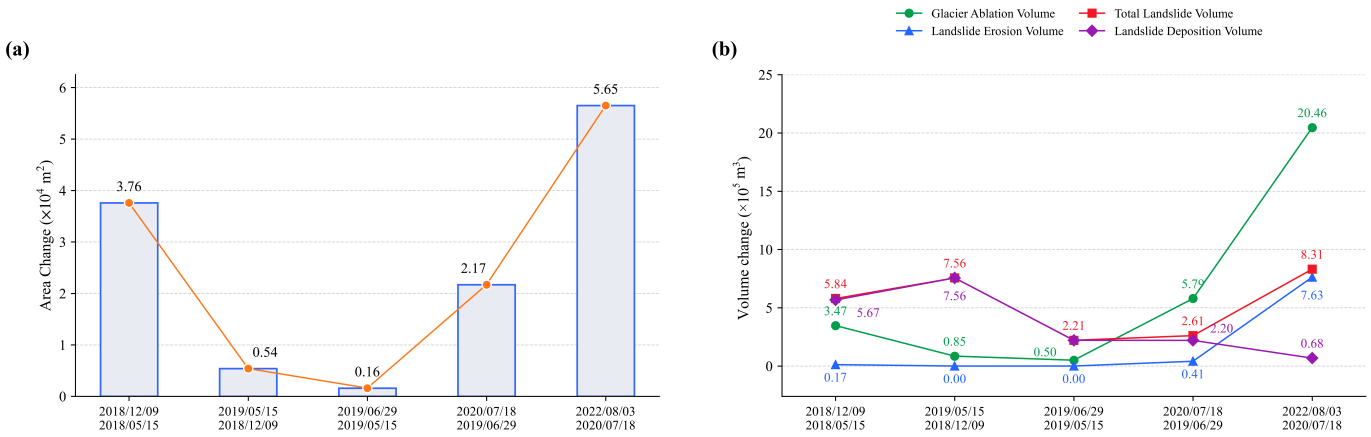

Figure 4. Glacier and landslide changes between successive monitoring intervals. (**a**) Glacier terminus area loss (×10⁴ m²); (**b**) glacier ablation, landslide deposition, landslide erosion, and total landslide volume change (×10⁵ m³). Total landslide change is deposition plus the positive erosion magnitude, distinct from net change (deposition minus erosion).

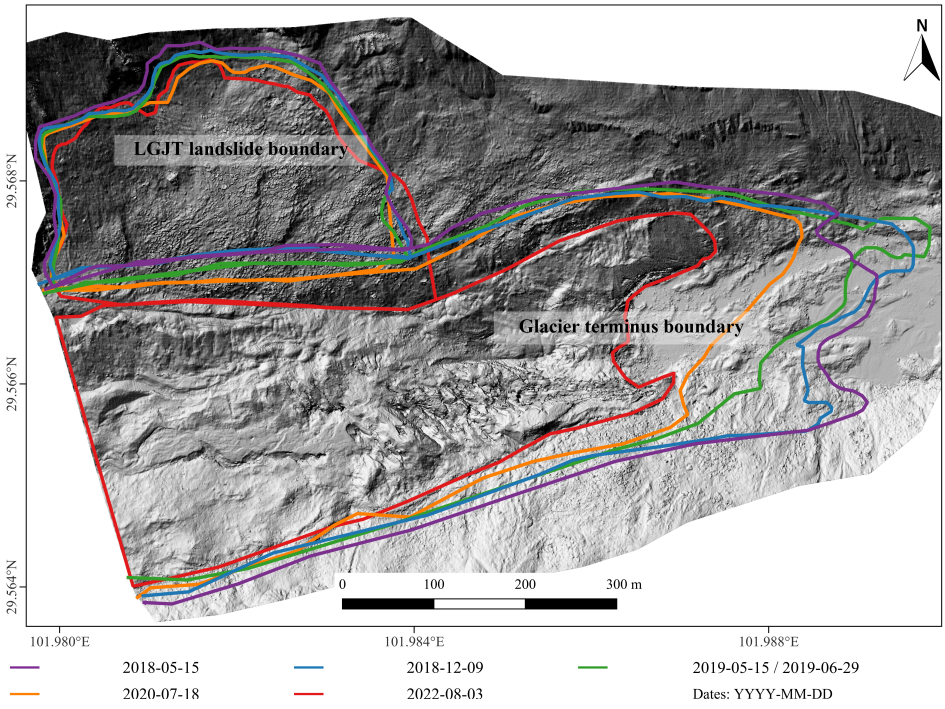

Figure 5. Glacier terminus and LGJT landslide boundaries from 2018 to 2022 overlaid on the 2022 hillshade. Colored lines represent the dates identified in the legend. The May and June 2019 outlines share green because they substantially overlap at this display scale, not because change was absent. Long straight closing segments delimit the selected analysis polygons and are not necessarily natural ice margins or landslide scarps. Boundaries were interpreted jointly from DOMs, DEMs, and three-dimensional models, including debris-covered glacier and moraine morphology.

Table 4. Annualized glacier and landslide change rates in adjacent periods.

Interval	Days (d)	Glacier Area Loss Rate ($\times 10^4$ m^2 a^{-1})	Glacier Volume Ablation Rate ($\times 10^5$ m^3 a^{-1})	Landslide Deposition Volume Rate ($\times 10^5$ m^3 a^{-1})	Landslide Erosion Volume Rate ($\times 10^4$ m^3 a^{-1})	Net Landslide Volume Change Rate ($\times 10^5$ m^3 a^{-1})
15 May 2018 to 9 December 2018	208	6.60	6.07	9.95	2.96	9.65
9 December 2018 to 15 May 2019	157	1.26	1.98	17.59	0.09	17.58
15 May 2019 to 29 June 2019	45	1.30	4.23	17.96	0.04	17.95
29 June 2019 to 18 July 2020	385	2.06	5.49	2.13	3.89	1.74
18 July 2020 to 3 August 2022	746	2.77	10.00	0.34	37.30	−3.39

Note: The symbol a denotes year. Area rates and landslide erosion volume rates are scaled by 10^4; the other volume rates are scaled by 10^5, as indicated in the column headers. Glacier volume ablation and landslide erosion are positive magnitudes. Net change is deposition minus erosion, $V_{net} = V_{dep} - V_{ero}$, after accounting for the different display scales; negative values indicate net surface-volume loss.

3.2. Landslide Volume Change

Glacier terminus retreat and landslide volume change exhibited distinct stage-dependent patterns during the monitoring period. The multi-temporal boundaries show that glacier retreat was spatially heterogeneous and was concentrated mainly in the low-lying frontal sector and along the lateral margin adjacent to the LGJT landslide. From May 2018 to August 2022, the delineated glacier terminus area decreased from 2.63×10^5 m^2 to 1.43×10^5 m^2, corresponding to an overall reduction of 45.5%. Although the largest absolute area loss occurred from July 2020 to August 2022, the annualized results in Table 4 show that the highest area loss rate occurred from May to December 2018. Therefore, the boundary evolution does not indicate a continuous acceleration of planimetric retreat. In contrast, glacier volume ablation intensified markedly during the final interval, reaching 2.046×10^6 m^3, with an annualized rate of 1.00×10^6 m^3 a^{-1}. The contrast between the area and volume change rates suggests that late-stage glacier degradation was increasingly characterized by pronounced surface lowering and vertical ice loss rather than solely by horizontal boundary recession.

The LGJT landslide simultaneously underwent a transition from deposition-dominated adjustment to erosion-dominated sediment export. From May 2018 to May 2019, LoD-filtered deposition was substantially greater than erosion, indicating that surface accumulation and internal redistribution dominated the landslide zone. Despite its short duration of only 45 days, the interval from May to June 2019 also exhibited a high annualized deposition rate, demonstrating intense short-term slope adjustment. From June 2019 to July 2020, the landslide retained a positive net volume balance, although erosion became more evident. A marked transition occurred from July 2020 to August 2022, when the erosion volume increased to 7.63×10^5 m^3, whereas deposition decreased to 6.80×10^4 m^3, producing a net volume change of -6.95×10^5 m^3. The corresponding annualized erosion and net change rates were 3.73×10^5 and -3.39×10^5 m^3 a^{-1}, respectively. These results demonstrate that late-stage landslide evolution was dominated by enhanced erosion and outward sediment transport, consistent with intensified channel incision and evacuation of previously accumulated material. Table 4 presents the annualized change

rates normalized by monitoring duration, allowing activity intensity to be compared among intervals of different lengths.

4. Discussion

4.1. Reliability and Uncertainty of LiDAR-Constrained Analysis

The reliability of multi-temporal DEM differencing depends critically on the quantification of co-registration errors over relatively stable reference areas and their propagation into geomorphic change estimates. For the synchronous 2022 datasets, the RMSE, NMAD, and mean elevation difference between the UAV-derived DEM and the airborne LiDAR DEM over relatively stable reference areas were 0.218, 0.144, and 0.087 m, respectively. The small mean bias and relatively low dispersion indicate good vertical consistency between the two independently acquired elevation datasets and support the use of the LiDAR DEM as an elevation reference. This agreement characterizes the synchronous 2022 comparison, but does not independently establish the accuracy of each historical DEM.

The elevation difference distributions over relatively stable reference areas nevertheless exhibited stage-dependent offsets and variations in dispersion (Figure 6). The earlier intervals were characterized by relatively compact central distributions and negligible tail proportions, whereas the comparisons for 2019 to 2020 and 2020 to 2022 contained broader distributions and small proportions of long-tail values. These patterns reflect interval-specific offsets and residual variability, which may arise from reconstruction and registration errors as well as minor surface changes within the relatively stable reference areas. Accordingly, the mean elevation difference over the relatively stable reference areas, μ_s, was removed from each DEM of Difference to correct the period-specific vertical bias. Subsequently, only pixels satisfying $|\Delta h_i| > \mathrm{LoD}_{95}$ were retained for glacier ablation and landslide erosion/deposition calculations, thereby limiting the contribution of weak, uncertainty-dominated elevation changes to the integrated volumes.

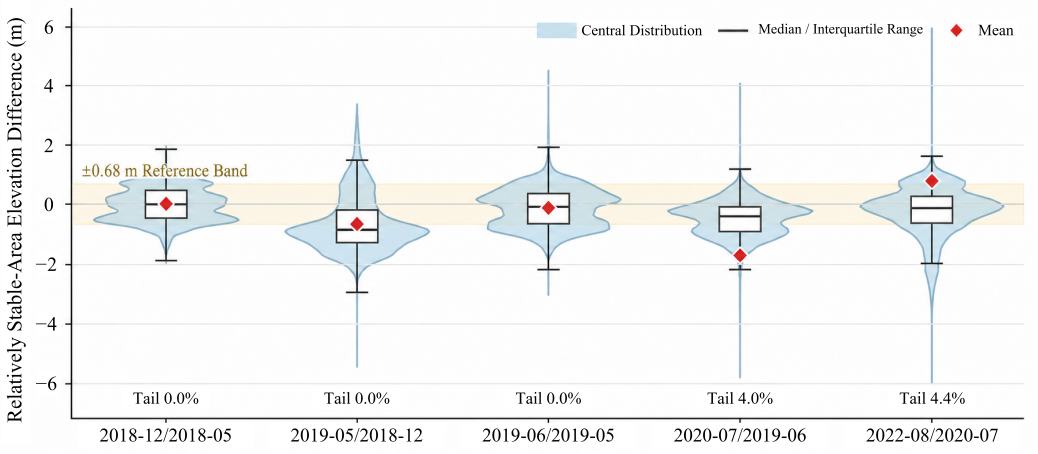

Figure 6. Elevation residual distributions over relatively stable reference areas for adjacent DEM pairs. Violin shapes show the displayed distributions, boxes show interquartile ranges, central lines indicate medians, and red diamonds indicate means. The shaded ±0.68 m band is a displayed reference band, not an established common LoD_{95} for all intervals.

The remaining uncertainties are likely associated with low image texture, terrain shadow, water-covered surfaces, topographic occlusion, and photogrammetric matching instability near rapidly changing glacier and landslide boundaries. Area estimates are additionally subject to uncertainty in manual boundary delineation. The reported volumes should therefore be interpreted as estimates of detectable surface change constrained by

uncertainty assessed over relatively stable reference areas and LoD_{95} screening, rather than exact sediment or ice volume balances.

4.2. Stage-Dependent Covariation and Geomorphic Interpretation

The DoDs show spatially concentrated surface lowering along the glacier terminus, the adjacent landslide margin, and channel corridors, while surface raising is more evident at the landslide toe and local deposition sites (Figure 7). The earlier intervals contain comparatively scattered patches of change. During July 2020–August 2022, negative elevation differences become more extensive near the glacier–landslide contact and within the adjoining slope. Their proximity to the retreating ice margin provides spatial context for the concurrent increase in glacier volume loss and landslide erosion, but does not by itself identify the process responsible.

The spatial pattern of elevation change revealed by the DoDs further supports the stage-dependent geomorphic evolution described above. During the early monitoring periods, from 2018 to 2019, positive and negative elevation change zones were mainly isolated patches. Positive elevation changes occurred sporadically in the middle and lower landslide area, reflecting microtopographic infilling and local creep-related deposition. Negative elevation changes were limited to a few steep scarps and did not form a continuous erosion corridor. In the DoD for the period from July 2020 to August 2022, the spatial organization of geomorphic change was strongly reorganized. Negative elevation changes, shown in deep red, became intense, extensive, and spatially continuous. Spatial overlay analysis indicated that strong negative changes were mainly associated with three geomorphic units: widespread vertical lowering caused by ice ablation and scarp retreat, physically unstable areas related to the failure of moraine ridges and the loss of lateral support, and main transport pathways formed by hydraulic erosion and lateral channel incision. In contrast, positive elevation changes, shown as blue areas, were greatly reduced and remained only at the frontal landslide toe and a few downstream deposition sites. This pattern of strong incision in the upper and middle reaches, glacier retreat at the terminus, and narrowed downstream deposition records a cascading geomorphic response after the landslide lost basal or lateral ice support. However, the available interval-integrated maps cannot separate loss of ice support, runoff erosion, and slope movement, or establish their temporal ordering.

The local minimum elevation change in the DoD for July 2020 to August 2022 was approximately −60.89 m (Figure 7e). This value represents an extreme local surface elevation difference rather than the mean thinning of the glacier terminus. Xu et al. [29] recorded an intense glacier terminus collapse at Hailuogou Glacier from 10 September to 5 November 2020, a period of only 56 days, with a local minimum elevation change of −41.83 m (approximately 40 m). This high-magnitude collapse event falls entirely within the July 2020 to August 2022 monitoring window of the present study. Therefore, the approximately −60.89 m extreme value extracted from the DoD is geomorphologically plausible in magnitude. Physically, it represents a cumulative compound signal produced by large-scale terminus collapse in 2020, subsequent surface melting, retreat of the ice cliff, and the exposure of the low-lying valley floor.

Annualized change-rate correlations provided a complementary description of the stage-dependent geomorphic patterns (Figure 8). The glacier volume ablation rate covaried positively with the landslide erosion volume rate (Pearson's $r = 0.89$; Spearman's $\rho = 0.80$) and negatively with the net landslide volume change rate ($r = -0.87$; $\rho = -0.80$). Thus, intervals of greater glacier volume loss generally coincided with enhanced erosion and a shift toward net material loss. These associations were consistent with the geomorphic transition from July 2020 to August 2022, when glacier ablation and landslide erosion reached

their highest annualized rates. Continued terminus retreat may have reduced lateral and frontal ice support while exposing unconsolidated moraine and toe materials. Concurrent changes in meltwater routing may have promoted channel incision and downslope sediment transport, providing a plausible physical context for the observed covariation.

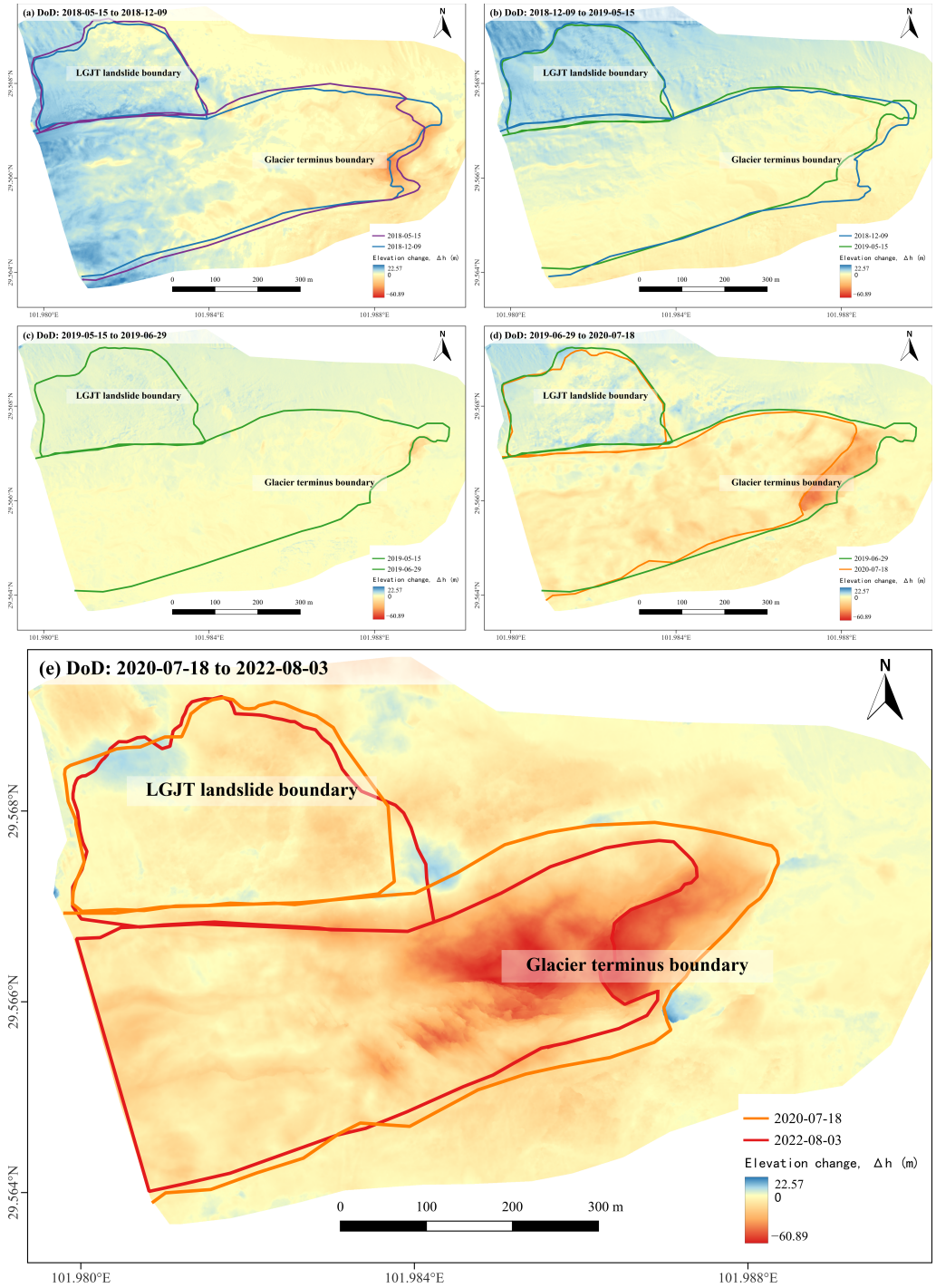

Figure 7. DoD-derived surface elevation changes, read left to right and top to bottom. (**a**) 15 May–9 December 2018; (**b**) 9 December 2018–15 May 2019; (**c**) 15 May–29 June 2019; (**d**) 29 June 2019–18 July 2020; (**e**) 18 July 2020–3 August 2022 (bottom panel). All panels use the same displayed elevation-change range, −60.89 to 22.57 m. Warm colors indicate lowering and cool colors indicate raising; the near-zero color does not independently establish a significance threshold. Outlines identify the mapped glacier and landslide domains. Elevation changes are interval totals, not annualized rates or three-dimensional displacement vectors.

These associations should nevertheless be interpreted cautiously because only five monitoring intervals were available ($n = 5$), limiting statistical power and the robustness of significance assessments. The final interval may exert substantial influence on the correlations. Annualization facilitates comparison across the 45–746-day intervals but does not equalize their seasonal and event coverage, particularly for the 45-day interval. Interpretation consequently places greater emphasis on consistency with DoD spatial patterns, DOM-derived boundary changes, and plausible physical and geomorphological processes than on statistical significance alone. Together with the potential effects of precipitation, freeze–thaw processes, slope structure, sediment availability, and antecedent deposition, these limitations support treating the correlations as exploratory evidence of stage-dependent covariation rather than a quantified coupling or direct causal response.

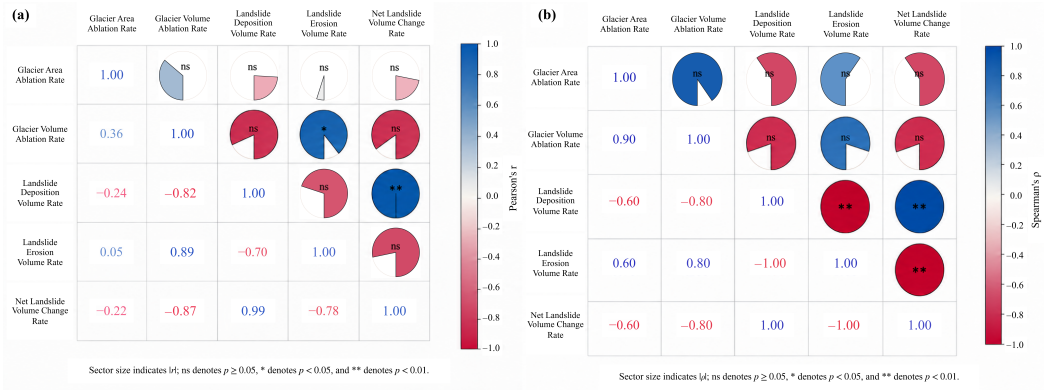

Figure 8. Correlation matrices of annualized glacier and landslide change rates across five adjacent intervals ($n = 5$). (**a**) Pearson coefficients; (**b**) Spearman rank coefficients. Lower triangles report coefficients; upper triangles encode direction by color and absolute magnitude by sector size. The supplied graphic retains ns ($p \geq 0.05$), * ($p < 0.05$), and ** ($p < 0.01$).

4.3. Precipitation Context and Possible Additional Controls

To assess the meteorological context of enhanced erosion and ice-avalanche occurrence during the final monitoring interval, we used ChinaMet monthly precipitation and mean air temperature data at a spatial resolution of 0.1°, obtained from the National Cryosphere Desert Data Center [32]. Area-averaged monthly precipitation and temperature were calculated using the overlap areas between the study-area polygon and the meteorological grid cells. Records from August 2020 to July 2022 were compared with the corresponding calendar-month climatology for 1991–2020. Total precipitation over these 24 complete months was 2189.6 mm, 2.75% above the climatological total, whereas mean temperature was 4.90 °C, 0.30 °C below the corresponding climatological mean. During the September–November 2020 ice-avalanche occurrence window, total precipitation was 192.7 mm, 16.65% below the historical seasonal mean, while mean temperature was 6.61 °C, 0.48 °C above the corresponding climatological mean temperature. September temperature was close to its climatological mean, whereas October and November were warmer by 0.54 and 0.86 °C, respectively; none of these three months exceeded the 90th percentile for its corresponding calendar month. Subsequently, precipitation in April and June 2022 was 33.1% and 32.9% above the respective climatological means, exceeding the corresponding 90th and 95th percentiles. Temperatures in March and July 2022 were higher by 2.46 and 1.07 °C, respectively, and both exceeded their calendar-month 95th percentiles. These results indicate that averages over the full interval obscured meteorological anomalies in individual months, and that warmer and wetter anomalies did not occur in the same months.

The ice-avalanche occurrence window was relatively warm and dry at the monthly scale, providing no evidence of an overall unusually wet period. Relatively warm conditions may have favoured ice melt and meltwater supply, providing a meteorological context for changes in ice stability. Wetter months following the ice avalanche may have promoted erosion and remobilization of loose material following glacier retreat and slope disturbance. Precipitation and temperature can therefore be considered potential influences on the terrain changes observed during the final monitoring interval. However, monthly meteorological data and interval-based DEM differencing cannot resolve short-term weather events or the detailed timing of terrain changes. They therefore cannot identify meteorological triggers of the ice avalanche or quantify the relative contributions of precipitation, temperature, and glacier change.

5. Conclusions

Based on six UAV photogrammetric surveys acquired between 2018 and 2022 and synchronous airborne LiDAR observations collected in 2022, this study applied an integrated LiDAR-constrained workflow to characterize the evolution of the Hailuogou glacier terminus and the adjacent LGJT landslide. Reference features, synchronous UAV–LiDAR comparison, and residual-based detection thresholds provide complementary constraints on relative surface-change estimates. Their usefulness remains conditional on feature identification, reference-area suitability, and the treatment of residual errors; they do not establish error-free alignment or independent accuracy for every historical epoch.

The glacier terminus monitoring zone underwent substantial but spatially heterogeneous retreat. Its area decreased from 2.63×10^5 m^2 in May 2018 to 1.43×10^5 m^2 in August 2022, corresponding to an overall area loss of approximately 1.20×10^5 m^2, or 45.5%. Boundary migration was concentrated primarily in the low-lying frontal sector and along the lateral margin adjacent to the landslide zone. From July 2020 to August 2022, the annualized glacier volume ablation rate reached 1.00×10^6 m^3 a^{-1}, indicating that late-stage glacier degradation was increasingly characterized by pronounced surface lowering and vertical ice loss rather than solely by horizontal terminus recession. The LGJT landslide exhibited a corresponding stage-dependent transition. From 2018 to 2019, its volumetric evolution was dominated by deposition, surface accumulation, and internal material redistribution. After July 2020, erosion and outward sediment transport became dominant. During the final monitoring interval, the annualized landslide erosion rate increased to 3.73×10^5 m^3 a^{-1}, while the net landslide volume change rate decreased to -3.39×10^5 m^3 a^{-1}. The annualized rate correlations and spatial DoD patterns consistently show that greater glacier volume ablation was accompanied by enhanced landslide erosion and increasingly negative net volume change. Given the limited number of monitoring intervals, however, these relationships should be interpreted as evidence of stage-dependent covariation and a plausible geomorphic linkage rather than proof of direct causation.

This study was limited by its reliance on manually delineated boundaries derived from DOM products to characterize planimetric glacier retreat and landslide activity. Continuous slope displacement fields were not available, and the possible effects of precipitation, meltwater discharge, freeze-thaw processes, and antecedent sediment storage could not be quantified directly. Multi-temporal synthetic aperture radar (SAR) observations can be used to monitor glacier motion and slope deformation through pixel-offset tracking and interferometry. At Hailuogou, Liu et al. [30] demonstrated these capabilities using satellite SAR, complemented by ground-based SAR observations of short-term landslide deformation. SAR-based monitoring could thus provide complementary evidence of glacier–landslide covariation, but displacement measurements alone do not directly reproduce the erosion and deposition volumes estimated from DoDs. Future studies should

integrate UAV surveys at a higher frequency, satellite and ground-based SAR observations, continuous meteorological and hydrological records, and in situ slope displacement measurements to better resolve the temporal response of landslide activity to glacier degradation and distinguish glacier-related effects from other environmental controls.

Supplementary Materials: The following supporting information can be downloaded at: https://www.mdpi.com/article/10.3390/rs18213841/s1, Figure S1: Multi-temporal views of the available reference features across all six surveys.

Author Contributions: Conceptualization, J.C. and J.Z.; methodology, J.Z.; software, W.Z. and Q.Z.; validation, M.L. and Y.Y.; formal analysis, J.Z. and L.H.; investigation, J.C., M.L., Y.Y. and L.H.; resources, Y.D.; data curation, J.Z. and L.H.; writing—original draft preparation, J.Z.; writing—review and editing, J.C. and B.Z.; visualization, J.Z. and W.Z.; supervision, J.C.; project administration, J.C.; funding acquisition, J.C. and Y.D. All authors have read and agreed to the published version of the manuscript.

Funding: This research was funded by the Central Government Guided Local Science and Technology Development Fund Projects (202502ZYDF034), the National Natural Science Foundation of China (Grant Nos. 42401101 and 42674106), the Science and Technology Program of the Geological Institution of Hunan Province (HNGYSTP202647), the Youth Fund Project of Humanities and Social Sciences Research of the Ministry of Education of China (25YJCZH106), the Technology Innovation Center for Emergency Surveying and Mapping, MNR (YJCX-2026-YB-03-01), and the Science and Technology Plan Projects of the Tibet Autonomous Region (XZ202601ZD0009).

Institutional Review Board Statement: Not applicable.

Informed Consent Statement: Not applicable.

Data Availability Statement: The data used in this paper are available from the first and corresponding authors upon reasonable request.

Acknowledgments: The authors would like to thank the Hailuogou Scenic Spot Management Bureau for granting permission to acquire UAV photogrammetric data and facilitating site access.

Conflicts of Interest: Authors Yixiang Du and Mingjun Li were employed by the company Sichuan Zhentong Inspection Co., Ltd. The remaining authors declare that the research was conducted in the absence of any commercial or financial relationships that could be construed as a potential conflict of interest.

Abbreviations

The following abbreviations are used in this manuscript:

DEM	digital elevation model
DoD	digital elevation model of difference
LGJT	Laoguanjingtai
LiDAR	Light detection and ranging
NMAD	Normalized median absolute deviation
SMRF	Simple morphological filter
RMSE	Root mean square error
UAV	Unmanned aerial vehicle

References

1. Zemp, M.; Jakob, L.; Dussaillant, I.; Nussbaumer, S.U.; Gourmelen, N.; Dubber, S.; A, G.; Abdullahi, S.; Andreassen, L.M.; Berthier, E.; et al. Community estimate of global glacier mass changes from 2000 to 2023. *Nature* **2025**, *639*, 382–388. [CrossRef] [PubMed]
2. Zekollari, H.; Schuster, L.; Maussion, F.; Hock, R.; Marzeion, B.; Rounce, D.R.; Compagno, L.; Fujita, K.; Huss, M.; James, M.; et al. Glacier preservation doubled by limiting warming to 1.5 C versus 2.7 C. *Science* **2025**, *388*, 979–983. [CrossRef] [PubMed]

3. Bhattacharya, A.; Bolch, T.; Mukherjee, K.; King, O.; Menounos, B.; Kapitsa, V.; Neckel, N.; Yang, W.; Yao, T. High Mountain Asian glacier response to climate revealed by multi-temporal satellite observations since the 1960s. *Nat. Commun.* **2021**, *12*, 4133. [CrossRef] [PubMed]
4. Lacroix, P.; Belart, J.M.C.; Berthier, E.; Saemundsson, T.; Jonsdottir, K. Mechanisms of Landslide Destabilization Induced by Glacier-Retreat on Tungnakvislarjokull Area, Iceland. *Geophys. Res. Lett.* **2022**, *49*, e2022GL098302. [CrossRef]
5. Zhang, G.; Carrivick, J.L.; Emmer, A.; Shugar, D.H.; Veh, G.; Wang, X.; Labedz, C.; Mergili, M.; Mölg, N.; Huss, M.; et al. Characteristics and changes of glacial lakes and outburst floods. *Nat. Rev. Earth Environ.* **2024**, *5*, 447–462. [CrossRef]
6. Zhang, T.; Yin, Y.; Li, B.; Liu, X.; Wang, M.; Gao, Y.; Wan, J.; Gnyawali, K.R. Characteristics and Dynamic Analysis of the February 2021 Long-Runout Disaster Chain Triggered by Massive Rock and Ice Avalanche at Chamoli, Indian Himalaya. *J. Rock Mech. Geotech. Eng.* **2023**, *15*, 296–308. [CrossRef]
7. Zhang, B.; Zhang, R.; Liu, G.; Liu, Q.; Cai, J.; Yu, B.; Fu, Y.; Li, Z. Monitoring of interannual variabilities and outburst regularities analysis of glacial lakes at the end of Gongba Glacier utilizing SAR images. *Geomat. Inf. Sci. Wuhan Univ.* **2019**, *44*, 1054–1064.
8. Wang, X.; Liu, L.; Hu, Y.; Wu, T.; Zhao, L.; Liu, Q.; Zhang, R.; Zhang, B.; Liu, G. Multi-Decadal Geomorphic Changes of a Low-Angle Valley Glacier in the East Kunlun Mountains: Remote Sensing Observations and Detachment Hazard Assessment. *Nat. Hazards Earth Syst. Sci.* **2021**, *21*, 2791–2810. [CrossRef]
9. Sattar, A.; Cook, K.L.; Rai, S.K.; Berthier, E.; Allen, S.; Rinzin, S.; de Vries, M.V.W.; Haeberli, W.; Kushwaha, P.; Shugar, D.H.; et al. The Sikkim flood of October 2023: Drivers, causes, and impacts of a multihazard cascade. *Science* **2025**, *387*, eads2659. [CrossRef] [PubMed]
10. He, H.; Ming, Z.; Zhang, J.; Wang, L.; Yang, R.; Chen, T.; Zhou, F. Robust estimation of landslide displacement from multitemporal UAV photogrammetry-derived point clouds. *IEEE J. Sel. Top. Appl. Earth Obs. Remote Sens.* **2024**, *17*, 6627–6641. [CrossRef]
11. Gracchi, T.; Rossi, G.; Tacconi Stefanelli, C.; Tanteri, L.; Pozzani, R.; Moretti, S. Tracking the evolution of riverbed morphology on the basis of UAV photogrammetry. *Remote Sens.* **2021**, *13*, 829. [CrossRef]
12. Benoit, L.; Gourdon, A.; Vallat, R.; Irarrazaval, I.; Gravey, M.; Lehmann, B.; Prasicek, G.; Gräff, D.; Herman, F.; Mariethoz, G. A high-resolution image time series of the Gorner Glacier–Swiss Alps–derived from repeated unmanned aerial vehicle surveys. *Earth Syst. Sci. Data* **2019**, *11*, 579–588. [CrossRef]
13. Karimi, N.; Sheshangosht, S.; Roozbahani, R. High-resolution monitoring of debris-covered glacier mass budget and flow velocity using repeated UAV photogrammetry in Iran. *Geomorphology* **2021**, *389*, 107855. [CrossRef]
14. Selbesoğlu, M.O.; Karabulut, M.F.; Oktar, Ö.; Akpinar, B.; Vassilev, O.; Arkali, M.; Tufan, Ş.N.; Ayyildiz, A.Ş.; Günaydin, E.; Yilmaz, A.; et al. Accuracy assessment of glacier depth monitoring based on UAV-GPR on Horseshoe Island, Antarctica. *Turk. J. Earth Sci.* **2023**, *32*, 999–1012. [CrossRef]
15. Hussain, Y.; Schlögel, R.; Innocenti, A.; Hamza, O.; Iannucci, R.; Martino, S.; Havenith, H.B. Review on the geophysical and UAV-based methods applied to landslides. *Remote Sens.* **2022**, *14*, 4564. [CrossRef]
16. Zhao, C.; Wang, M.; Yin, Y.; Tie, Y.; Zhu, S.; Liang, J.; Zhang, S.; Feng, J.; Song, B.; Li, X. Landslide Deformation Remote Monitoring in Alpine Mountains Using UAV Photogrammetry and Infrared Thermography: A Case Study in Wumeng Mountain Region, China. *Remote Sens.* **2026**, *18*, 1961. [CrossRef]
17. Du, P.; Xu, Y.; Guo, Y.; Li, H. Assessing loess landslide volume using high-precision UAV-derived DEM: A case study of the 15 March 2019 landslide in Zaoling Township, Xiangning County in North China. *Nat. Hazards Res.* **2023**, *3*, 640–645. [CrossRef]
18. Yordanov, V.; Truong, Q.X.; Brovelli, M.A. Estimating landslide surface displacement by combining low-cost UAV setup, topographic visualization and computer vision techniques. *Drones* **2023**, *7*, 85. [CrossRef]
19. Yang, L.; Cui, Y.; Xu, C.; Ma, S. Application of coupling physics–based model TRIGRS with random forest in rainfall-induced landslide-susceptibility assessment: Yang, Cui, Xu and Ma. *Landslides* **2024**, *21*, 2179–2193.
20. Zhang, L.; Zhang, R.; Dou, J.; Hou, S.; Xiang, Z.; Wang, H.; Yang, P.; Liu, X. Advancing reservoir landslide stability assessment via TS-InSAR and airborne LiDAR observations in the Daping landslide group, Three Gorges Reservoir Area, China: L. Zhang et al. *Landslides* **2025**, *22*, 169–188. [CrossRef]
21. Cheng, Z.; Gong, W.; Tang, H.; Juang, C.H.; Deng, Q.; Chen, J.; Ye, X. UAV Photogrammetry-Based Remote Sensing and Preliminary Assessment of the Behavior of a Landslide in Guizhou, China. *Eng. Geol.* **2021**, *289*, 106172. [CrossRef]
22. Ilinca, V.; Sandric, I.; Chitu, Z.; Irimia, R.; Gheuca, I. UAV Applications to Assess Short-Term Dynamics of Slow-Moving Landslides under Dense Forest Cover. *Landslides* **2022**, *19*, 1717–1734. [CrossRef]
23. Santo, A.; Marino, E.; Valente, E.; Massaro, L. Analysis of slow-moving landslide evolution using high-resolution UAV monitoring: The Pietrapertosa earthflow (Southern Apennines, Italy). *Landslides* **2026**, *23*, 3227–3246. [CrossRef]
24. Zhou, J.; Jiang, N.; Li, C.; Li, H. A Landslide Monitoring Method Using Data from Unmanned Aerial Vehicle and Terrestrial Laser Scanning with Insufficient and Inaccurate Ground Control Points. *J. Rock Mech. Geotech. Eng.* **2024**, *16*, 4125–4140. [CrossRef]
25. Yang, J.; Liu, Q.; Luo, Y.; Yin, Y.; Lu, X. Rapid dynamics of paraglacial vegetation under temperate deglaciating environments in Mt. Gongga, southeastern Tibetan Plateau. *J. Geogr. Sci.* **2025**, *35*, 1979–1997. [CrossRef]

26. Dan, Z.; Zhang, Z.; Zhang, Q. Remote sensing monitoring of Hailuogou Glacier change from 1974 to 2020. *J. Glaciol. Geocryol.* **2023**, *45*, 1276–1287.
27. Liao, H.; Liu, Q.; Zhong, Y.; Lu, X. Supraglacial debris-cover change and its spatial heterogeneity in the Mount Gongga, 1990–2019. *Acta Geogr. Sin.* **2021**, *76*, 2647–2659.
28. Wang, H.; Liu, Q.; Zhong, Y.; Luo, Y. A dataset of glacier crevasse distribution in the ablation areas of Hailuogou Glacier, Mt. Gongga (2016–2021). *China Sci. Data* **2022**, *7*, 255703234. [CrossRef]
29. Xu, S.; Fu, P.; Quincey, D.; Feng, M.; Marsh, S.; Liu, Q. UAV-based geomorphological evolution of the Terminus Area of the Hailuogou Glacier, Southeastern Tibetan Plateau between 2017 and 2020. *Geomorphology* **2022**, *411*, 108293. [CrossRef]
30. Liu, G.; Zhang, B.; Zhang, R.; Cai, J.; Fu, Y.; Liu, Q.; Yu, B.; LI, Z. Monitoring dynamics of Hailuogou glacier and the secondary landslide disasters based on combination of satellite SAR and ground-based SAR. *Geomat. Inf. Sci. Wuhan Univ.* **2019**, *44*, 980–995.
31. Pingel, T.J.; Clarke, K.C.; McBride, W.A. An improved simple morphological filter for the terrain classification of airborne LIDAR data. *ISPRS J. Photogramm. Remote Sens.* **2013**, *77*, 21–30. [CrossRef]
32. Hu, Y.; Zhang, L. Added value of merging techniques in precipitation estimates relative to gauge-interpolation algorithms of varying complexity. *J. Hydrol.* **2024**, *645*, 132214. [CrossRef]

Disclaimer/Publisher's Note: The statements, opinions and data contained in all publications are solely those of the individual author(s) and contributor(s) and not of MDPI and/or the editor(s). MDPI and/or the editor(s) disclaim responsibility for any injury to people or property resulting from any ideas, methods, instructions or products referred to in the content.